scientific reports

Check for updates

OPEN

Inhibition of epigenetic and cell cycle-related targets in glioblastoma cell lines reveals that onametostat reduces proliferation and viability in both normoxic and hypoxic conditions

Darja Lavogina[1,2,3]✉, Mattias Kaspar Krõlov[2], Hans Vellama[4,5], Vijayachitra Modhukur[3,6], Valentina Di Nisio[7,8], Helen Lust[1], Kattri-Liis Eskla[4,5], Andres Salumets[3,6,7,8] & Jana Jaal[1,9]✉

The choice of targeted therapies for treatment of glioblastoma patients is currently limited, and most glioblastoma patients die from the disease recurrence. Thus, systematic studies in simplified model systems are required to pinpoint the choice of targets for further exploration in clinical settings. Here, we report screening of 5 compounds targeting epigenetic writers or erasers and 6 compounds targeting cell cycle-regulating protein kinases against 3 glioblastoma cell lines following incubation under normoxic or hypoxic conditions. The viability/proliferation assay indicated that PRMT5 inhibitor onametostat was endowed with high potency under both normoxic and hypoxic conditions in cell lines that are strongly MGMT-positive (T98-G), weakly MGMT-positive (U-251 MG), or MGMT-negative (U-87 MG). In U-251 MG and U-87 MG cells, onametostat also affected the spheroid formation at concentrations lower than the currently used chemotherapeutic drug lomustine. In T98-G cell line, treatment with onametostat led to dramatic changes in the transcriptome profile by inducing the cell cycle arrest, suppressing RNA splicing, and down-regulating several major glioblastoma cell survival pathways. Further validation by immunostaining in three cell lines confirmed that onametostat affects cell cycle and causes reduction in nucleolar protein levels. In this way, inhibition of epigenetic targets might represent a viable strategy for glioblastoma treatment even in the case of decreased chemo- and radiation sensitivity, although further studies in clinically more relevant models are required.

Glioblastoma (GB) is a highly aggressive and lethal form of brain cancer in adults. Despite the use of multiple treatment strategies, the prognosis remains poor. For nearly 2 decades, the standard treatment of patients with GB consists of surgery followed by radiochemotherapy that results in median overall survival time only up to 14.6 months[1]. Unfortunately, almost all GB patients experience rapid tumour recurrence, and there is no established standard of care for disease progression after radiotherapy and concomitant temozolomide. Lomustine, a

[1]Institute of Clinical Medicine, University of Tartu, L. Puusepa 8, 50406 Tartu, Estonia. [2]Chair of Bioorganic Chemistry, Institute of Chemistry, University of Tartu, Tartu, Estonia. [3]Competence Centre on Health Technologies, Tartu, Estonia. [4]Department of Physiology, Institute of Biomedicine and Translational Medicine, University of Tartu, Tartu, Estonia. [5]Centre of Excellence for Genomics and Translational Medicine, University of Tartu, Tartu, Estonia. [6]Department of Obstetrics and Gynecology, Institute of Clinical Medicine, University of Tartu, Tartu, Estonia. [7]Department of Gynecology and Reproductive Medicine, Karolinska University Hospital, Huddinge, Stockholm, Sweden. [8]Division of Obstetrics and Gynecology, Department of Clinical Science, Intervention and Technology, Karolinska Institutet, Huddinge, Stockholm, Sweden. [9]Department of Radiotherapy and Oncological Therapy, Tartu University Hospital, Tartu, Estonia. ✉email: darja.lavogina@ut.ee; jana.jaal@ut.ee

nitrosourea compound, is commonly used in chemotherapy when the disease recurs, based on several phase II and III studies that have reported median overall survival times ranging from 5.6 to 9.8 months[2–4]. Re-irradiation has also been shown to provide temporary disease control in recurrent GB patients[5]. Since GB is one of the most angiogenic tumours, angiogenesis inhibitors have also been widely tested. Out of these, vascular endothelial growth factor (VEGF) or its receptor (VEGFR) blockers, such as bevacizumab and regorafenib, have shown only modest efficacy[6,7].

As radiotherapy, chemotherapy, and angiogenesis inhibitors only result in temporary disease stabilization, additional, more targeted strategies for treating GB are needed. Although GB is a highly vascularized tumour, it is known that blood flow in these newly formed blood vessels is rather inefficient—which leads to the formation of large hypoxic areas and associated necrosis, one of the hallmarks of GB morphological diagnosis[8]. Therefore, from clinical point of view, the optimal new drug should be equally effective in oxygenated as well as in hypoxic tumour areas.

While numerous reports have investigated the efficiency of individual compounds in simplified model systems such as GB cell lines, few studies have focused on the systematic comparison of different pathways that define the characteristic viability profile of GB. Moreover, few publications have addressed in this context the importance of hypoxia—although it has been shown that the hypoxia-induced pathways affect metabolism, survival, and drug resistance mechanisms of GB cell lines, making hypoxic conditions relevant for screening putative drug candidates[9–11].

In a previous study, we screened 13 individual compounds and combinations thereof with temozolomide and lomustine using viability assay for the assessment of targeted modulation in GB cells[12]. The efficacy of targeted modulation of signalling pathways was compared in two GB cell lines, U-251 MG and T98-G. These cell lines differ in expression levels of O6-methylguanine-DNA methyltransferase (MGMT), which contributes to the resistance of cells to drugs that act via DNA alkylation: U-251 MG expresses low levels of MGMT, while T98-G expresses higher levels of MGMT and is more resistant to alkylating agents[13]. We found that among the choice of screened compounds, the inhibitors of Aurora family possessed the highest potency. In case of compound combinations, mixtures containing 5-azacytidine—an inhibitor of DNA methyltransferases (DNMT) 1 and 3—showed the most remarkable increase in potency as compared to the individual drugs.

Here, we carried out a follow-up study utilizing an expanded panel of inhibitors targeting the cell cycle-related kinases as well as several families of proteins responsible for epigenetic modifications. Out of 11 chosen compounds, 6 have been explored in clinical trials and 4 are approved for treatment of solid or haematological cancers (see Supplementary Table S1 for details). We also added a third GB cell line to the study, U-87 MG—the latter is MGMT-negative yet expresses the human apurinic/apyrimidinic endonuclease, which contributes to higher resistance of these cells to ionizing radiation[14]. The cell lines were incubated with the panel of compounds of interest in normoxic (20% oxygen) or in hypoxic conditions (1% oxygen). Based on the established viability/proliferation profiles, a PRMT5 inhibitor onametostat was identified as the new player of interest. The effect of onametostat was further explored using the spheroid formation assay, transcriptome studies, and immunofluorescent (IF) staining of the cell cycle-related or nucleolar markers in GB cells (Fig. 1).

Materials and methods

Cell lines, chemicals and equipment

Human glioblastoma cell lines T98-G, U-251 MG, and U-87 MG were from the American Type Culture Collection (ATCC; Manassas, VA, USA). Lomustine, barasertib (AZD1152-HQPA), CYC116, danusertib (PHA-739358), alisertib (MLN8237), MS023, onametostat (JNJ-64619178), palbociclib (PD-0332991) hydrogen

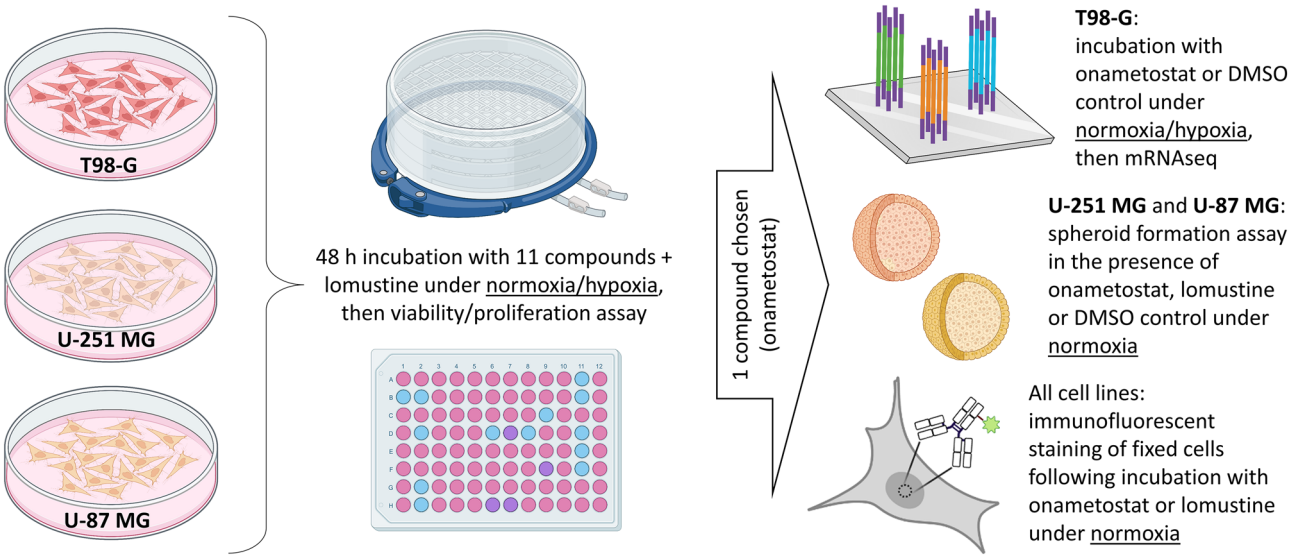

Figure 1. Workflow of the current project. The figure was composed using BioRender.

chloride salt, tazemetostat (EPZ-6438), and VX 689 (MK-5108) were obtained from Selleckchem (Munich, Germany). Azacytidine and vorinostat (suberanilohydroxamic acid or SAHA) were from Cayman Chemical (Ann Arbor, Michigan, United States). The stock solutions of compounds were prepared in cell culture grade DMSO was from AppliChem (Darmstadt, Germany) and stored at − 20 °C.

The solutions and growth medium components for the cell culture were obtained from the following sources: phosphate-buffered saline (PBS), fetal bovine serum (FBS)—Sigma-Aldrich (Steinheim, Germany); Eagle's Minimum Essential Medium (EMEM) modified to contain Earle's Balanced Salt Solution, non-essential amino acids, 2 mM L-glutamine, 1 mM sodium pyruvate, and 1500 mg/L sodium bicarbonate—ATCC (Manassas, VA, USA); a mixture of penicillin, streptomycin, and amphotericin B—Capricorn (Ebsdorfergrund, Germany). Resazurin and PBS for viability assay (supplemented with Ca^{2+}, Mg^{2+}) were from Sigma-Aldrich (St Louis, MO, USA). The propidium iodide for staining of spheroids was obtained from Acros Organics (Switzerland).

The cells were grown at 37 °C in 5% CO_2 humidified incubator (Sanyo; Osaka, Japan). For viability assay, the initial number of cells was counted using TC-10 cell counter (Bio-Rad; Hercules, CA, USA). In case of the viability assay, the cells were seeded onto transparent 96-well clear flat bottom cell culture plates BioLite 130188; during treatment of cells prior to mRNA sequencing, the cells were grown on the transparent 6-well clear flat bottom cell culture plates BioLite 130184 (both from Thermo Fischer Scientific, Rochester, NY, USA). In case of spheroid formation assay, 96-well black ultra-low attachment spheroid microplates with clear round bottom were used (Corning 4515; Kennebunk, ME, USA). In case of apoptosis assay or immunofluorescence studies, the cells were seeded, treated and imaged on 96-well tissue culture-treated Ibidi black µ-plates (ibidi GmbH, Gräfelfing, Germany).

For hypoxia studies, two different hypoxic chambers were used. In the first case, cultured cells were placed in the modular incubator chamber (Billups-Rothenberg Inc, MIC-101), a flow meter was attached to the unit and the chamber was flushed with 20 L of gas mixture (1% O_2, 5% CO_2, 94% N_2). The chamber was sealed and placed into the incubator (37 °C); the gas mixture was exchanged after every 24 h. In the second case, hypoxic gas mixture (1% O_2, 5% CO_2, 94% N_2) was supplied by gas controller into the incubator of Cytation 5 multi-mode reader system equilibrated at 37 °C (BioTek; Winooski, VT, USA).

For apoptosis assay, a previously developed FRET biosensor measuring caspase-3 activity was used combined with the baculovirus-based BacMam transduction system[15].

For fixation of cells and further procedures in IF experiments, methanol was obtained from Honeywell (Riedel-de Haën™, Seelze, Germany), BSA from Capricorn Scientific (Ebsdorfergrund, Germany), and PBS (supplemented with Ca^{2+}, Mg^{2+}) from Sigma-Aldrich (Steinheim, Germany). The following primary antibodies were used: rabbit polyclonal antibodies against human Aurora A (anti-AurA; HPA002636) or against human cyclin A2 (anti-CCNA2; HPA020626)—both obtained from Sigma-Aldrich (Saint Louis, Missouri, USA); rabbit polyclonal antibodies against phosho-serine 10 of human histone H3 (anti-pS10H3; ab5176), against human centromere protein F (anti-CENPF; ab5), or against human nucleolin (anti-NCL; ab70493)—all three obtained from Abcam (Cambridge, UK); rabbit monoclonal antibody against human nuclear mitotic apparatus protein (anti-NuMA; #8967)—obtained from Cell Signaling Technology (Danvers, Massachusetts, USA); and rabbit monoclonal antibody against monomethylated Arg3 of human histone H4 (anti-H4R3me1; MA5-24689)—obtained from Thermo Fisher Scientific (Waltham, Massachusetts, USA). The secondary antibody [goat pre-adsorbed antibody against rabbit IgG (H&L), conjugated with ATTO 647N; 611-156-122] was from Rockland Immunochemicals (Philadelphia, Pennsylvania, USA) and the nuclear stain 4′,6-diamidino-2-phenylindole (DAPI) was from Invitrogen (Eugene, Oregon, USA).

Fluorescence intensity and absorbance measurements were carried out with Synergy NEO or Cytation 5 multi-mode readers (both from BioTek; Winooski, VT, USA). Bright-field and fluorescence microscopy was carried out with Cytation 5 multi-mode reader using 4× air objective (1.613 µm/pixel) or 20× air objective (0.3225 µm/pixel) and automated focussing regime.

Viability/proliferation assay

T98-G, U-251 MG, or U-87 MG cells (passage number below 15) were seeded in growth medium onto the 96-well plate with the density of 2500, 3500 or 2000 cells per well, respectively (within the linear range of the method, optimized in previous studies[16] or shown in Supplementary Fig. S1). The cells were left to attach for 24 h at 37 °C in normoxic conditions (95% room air, 5% CO_2). Next, the growth medium was exchanged, and dilution series of biologically active compounds in PBS were added onto the cells (the final volume of PBS relative to the fetal bovine serum-containing growth medium was 1/10). Based on the solubility of compounds in the water, the following final total concentrations were chosen: azacytidine, lomustine, MS023, vorinostat—sixfold dilution starting from 50 µM; onametostat—sixfold dilution starting from 20 µM; CYC116, palbociclib, tazemetostat—sixfold dilution starting from 10 µM; alisertib, barasertib, danusertib, VX 689—sixfold dilution starting from 5 µM. In the case of onametostat and alisertib, additional dilution series were used for establishing more precise dose–response at low concentrations: starting from 0.3 to 200 nM, respectively. An identical volume of PBS was added to the negative control (100% viability). The final volume per well was 200 µL, and the concentration of DMSO in the treated wells was ≤ 0.1% by volume; on each plate, each concentration of each compound was represented in duplicate or triplicate. The cells were incubated for 48 h at 37 °C in normoxic or hypoxic conditions, and viability assay was then carried out according to the previously published protocol[16].

Spheroid formation assay

U-251 MG or U-87 MG cells (passage number below 10) were seeded in growth medium onto the 96-well ultra-low attachment plate with the density of 2500 (experiment 1), 2000 (experiment 2) or 1000 (experiment 3) cells per well. At the same time, dilutions of compounds in the growth medium were added to the wells. The final

total volume in the well was 200 µL and the final total concentrations were as follows: onametostat—20 µM, 2 µM, or 0.2 µM; lomustine—50 µM; DMSO—0.1% by volume (negative control). The plates were incubated for 48 h at 37 °C in normoxic conditions; next, half of the medium was then replaced with the fresh one (containing the same concentrations of the compounds as outlined above) and the incubation was continued. Following the 95-h incubation, solution of propidium iodide in PBS was added to all wells (final total concentration of 2 µg/mL) and the plates were incubated for 1 h. Finally, imaging was carried out (4× air objective) using bright-field (settings—LED intensity 5, integration time 100, detector gain 3) and RFP channel (settings—LED intensity 5, integration time 350, detector gain 15).

Transcriptome studies: sample preparation and mRNA sequencing

T98-G cells (passage number below 10) were seeded in growth medium onto the 6-well plates and grown to 80–85% confluency in normoxic conditions. Subsequently, solutions of onametostat (final total concentration of 1 µM) or DMSO (final total concentration of 0.1% by volume; negative control) in growth medium were prepared and added onto the cells. The treatment lasted for 48 h at 37 °C in normoxic or hypoxic conditions. Next, the medium was removed, the cells were briefly rinsed with PBS and then lysed using RLT buffer (350 µL per well; Qiagen, Hilden, Germany) from the RNeasy Mini kit (Qiagen, Hilden, Germany). The lysates were collected and stored at − 80 °C until further use.

The RNA extraction was performed using the RNeasy Mini Kit, together with DNase I treatment (Qiagen, Hilden, Germany), following the manufacturer's instructions. Afterwards, the RNA concentration of each sample was measured with Nanodrop (IMPLEN, Nordic Biolabs) and Agilent TapeStation QC (Agilent Technologies Inc., CA, USA). High-quality samples (A260/A280 > 1.8, and RNA integrity > 9) were selected for library preparation using the Illumina Stranded mRNA Prep Ligation protocol (Illumina, USA), following the manufacturer's instructions, and using 200 ng of RNA as input. The final library included 12 samples, and it was sequenced using the Illumina NextSeq2000 sequencing platform 100 cycle flow cell in Bioinformatics and Expression Analysis core facility (BEA) at Karolinska Institute, Sweden. For sequencing, 1000 pM of the library was loaded on the flow cell.

IF studies

U-251 MG, T-98G or U-87 MG cells (passage number below 10) were seeded in growth medium onto the 96-well microscopy plate with the density of 2000–8000 cells per well. The cells were left to attach for 24 h at 37 °C in normoxic conditions (95% room air, 5% CO_2). Next, the dilution series of biologically active compounds in growth medium were added. The following final total concentrations were chosen: onametostat—tenfold dilution starting from 20 µM, lomustine—50 µM; the final volume per well was 200 µL. The cells were incubated for 48 h at 37 °C in normoxic conditions. Subsequently, fixation, IF staining and DAPI staining of cells was carried out according to the previously published protocol[17]. The primary antibodies were used at the following dilutions: anti-pS3H10, 1:2000 (N = 6); anti-AurA, 1:500 (N = 3); anti-CCNA2, 1:120 (N = 3); anti-CENPF, 1:500 (N = 3); anti-NCL, 1:500 (N = 3); anti-NuMA, 1:300 (N = 6); anti-H4R3me1, 1:1000 (N = 4).

Finally, imaging was carried out (20× air objective) using DAPI channel (LED intensity 3, integration time 54, detector gain 5) and CY5 channel (LED intensity 7, integration time 926, detector gain 12 for all conditions except H4R3me1 staining that was imaged with LED intensity 9, integration time 350, detector gain 15). The imaging was performed in the automated mode; 25 images per well were taken and the DAPI channel was used for autofocusing.

Software

For general data analysis, GraphPad Prism 6 (San Diego, CA, USA) and Excel 2016 (Microsoft Office 365; Redmond, WA, USA) were used.

In case of the apoptosis assay, the image analysis was performed with Gen5 software (BioTek; Winooski, VT, USA). For U-251 MG and U-87 MG cells, minimal GFP channel intensity cut-off of 2000 and object size of 10–100 µm was applied, while for T-98G cells, minimal GFP channel intensity cut-off of 500 and object size of 10–200 µm was applied. In spheroid formation assay, ImageJ software (Fiji package[18]) was used for the image analysis.

In case of transcriptomic data, the RNA sequencing reads were initially assessed for quality using the FASTQC program (version 0.11.8) to ensure high quality data[19]. Based on the FASTQC results, MultiQC program was utilized to generate a comprehensive report on the sequencing data quality[20]. Subsequently, the reads underwent trimming using the Fastp program[21]. The trimmed reads were then aligned to the human reference genome GRCh38 using STAR 2.7.5a[22]. To estimate the read counts per gene, we utilized the featureCounts tool with default parameters[23]. The T-Distributed Stochastic Neighbor Embedding (t-SNE) technique was implemented for clustering analysis using the R package Rtsne[24]. Prior to t-SNE analysis, we applied the variance stabilizing transformation to the raw count data using the DeSeq2 Bioconductor package[25]. This transformation was carried out to eliminate potential biases and enhance the accuracy of the clustering analysis. Differential gene expression analysis was performed in the R environment using the edgeR 3.28 package[26].

To create the Venn diagram and the Volcano plots, we utilized the interactive tool Venny[27] and the Enhanced-Volcano R package[24], respectively. For analysis of the cellular pathways up- or downregulated in various treatment comparisons, an online platform Metascape was applied (version V3.5.20230501[28]).The automated analysis of IF images was carried out using the Ilastik model and the modified version of MembraneTools module of Aparecium 2.0 software[29] as reported previously[12].

Statistical analysis

Throughout the study, the grouped comparisons were carried out using one-way ANOVA with Dunnett's test for multiple comparisons; unless indicated otherwise, the pairwise comparisons were carried out using the unpaired two-tailed t-test with Welch's correction. In all statistical tests, the significance of comparisons is indicated as follows: *** indicates $P \le 0.001$, ** indicates $P \le 0.01$, * indicates $P \le 0.05$.

In case of viability assay, the data analysis was carried out according to the previously published protocol[16]. Specifically, in each independent experiment, the fluorescence intensity measured for the replicate treatments was pooled and the data obtained for the negative control was plotted against incubation time with resazurin. One time-point within duration of data acquisition was chosen where the signal of the negative control remained in the linear range, and only data measured at this time-point was used for the further analysis. For normalization, data obtained for wells treated with PBS (blank control) was considered as 100% viability; data acquired for the 50 µM resazurin solution (in the absence of cells) was considered as 0% viability. Next, the ratio of absorbance at 570 nm and 600 nm was calculated for each well. The ratios were analyzed analogously to the fluorescence intensity data, and the normalized viability values calculated from the fluorescence intensity and the absorbance measurements were pooled. Finally, data from all independent experiments ($N \ge 3$ for each treatment in each cell line) was pooled for each individual compound and oxygenation condition. The pooled normalized viability was plotted against the concentration of compound in the dilution series and fitted to the logarithmic dose–response function (three parameters), or to the biphasic equation with the Hill slope values fixed at − 1 and the fraction of the curve derived from the more potent phase fixed between 0 and 1.

In spheroid formation assay, the spheroid contour was denoted manually using the freehand selections tool and the area, diameter and circularity of the spheroid were quantified; in case of disintegrated spheroids with poorly defined borders, the selection involved all dark area covered with cells. For the RFP channel images, the average signal intensity of propidium iodide per unit of area was also established. The measured parameters were normalized to the negative control in the given cell line (set to 100%) in each independent experiment ($N = 2$ for each treatment), and the data for the identically treated cells within the same cell line was then pooled for all independent experiments.

In case of transcriptomic study, genes with low counts were filtered out prior to the differential gene expression analysis using the filterByExpr function from the edgeR package to ensure robust results. Genes with absolute log fold change $|\log FC| > 1$ and FDR-adjusted P-value (q-value) < 0.05 were considered as differentially expressed. In pathway enrichment analysis, all genes in the genome have been used as the enrichment background. Terms with a P-value < 0.01, a minimum count of 3, and an enrichment factor > 1.5 (the enrichment factor is the ratio between the observed counts and the counts expected by chance) were collected and grouped into clusters based on their membership similarities. The P-values were calculated based on the cumulative hypergeometric distribution.

The analysis of the raw IF data was carried out according to the previously established protocol[17]. The total intensity of antibody signal in nucleus was plotted by pooling data for all nuclei identified from the identically treated cells in all the independent experiments ($N = 4–6$). The normality of data distribution in each condition was tested using the D'Agostino-Pearson test and non-Gaussian distribution was confirmed for all tested conditions. Therefore, the statistical significance of pairwise comparison of the treatments of interest was carried out using the unpaired two-tailed Mann–Whitney U-test (95% confidence level).

Results

Viability profiling of GB cell lines following treatment in normoxic or hypoxic conditions

As the first step of our study, we established the viability/proliferation profiles of T98-G, U-251 MG and U-87 MG cell lines following the 48-h incubation with the set of twelve compounds under normoxic or hypoxic conditions. The compounds included 5 inhibitors of enzymes carrying out epigenetic modifications (including DNMT family, histone-lysine N-methyltransferase EZH2, protein arginine methyltransferase family PRMT, histone deacetylase family HDAC), 6 inhibitors of the cell cycle-related protein kinases (including Aurora and cyclin-dependent kinase CDK families), and a control compound lomustine. The details on the previously reported targets of the compounds of interest are listed in the Supplementary Table S1; apart from MS023, all compounds have been tested in clinical trials or approved for clinical use.

The negative logarithms of IC_{50} values (pIC_{50}) of compounds measured in the viability/proliferation assay are summarized in Table 1, and visualized as radar plots in Fig. 2 and Supplementary Fig. S2. The dose–response curves of individual compounds are shown in Supplementary Figs. S3–S5; additional parameters (apart from the IC_{50} values) obtained from the dose–response curves are compared in Supplementary Fig. S6. Overall, T98-G was found to be the least and U-87 MG the most chemosensitive cell line, yet the same compounds were identified as the most efficient in all cell lines tested: an Aurora A kinase inhibitor alisertib, and a PRMT5 inhibitor onametostat. Both compounds featured biphasic dose–response profile, with the low-dose IC_{50} values in low nanomolar to subnanomolar range. In accordance with the previous study[12], an Aurora A/B inhibitor barasertib was also found highly potent in U-251 MG cells.

The effect of hypoxia was relatively small, yet statistically significant differences in compound potency under hypoxic *vs* normoxic conditions were observed in several cases. According to the comparison of IC_{50} values, under hypoxic conditions the potency of 5-azacytidine was reduced in U-251 MG cells ($P < 0.01$) and the potency of vorinostat in U-87 MG cells ($P < 0.01$). The potency of tazemetostat was reduced in U-87 MG ($P < 0.05$) as well as in U-251 MG cells, but in the latter case, the exact IC_{50} value under hypoxic conditions was too high to measure with the assay used. On the other hand, increase of potency under hypoxic conditions could be observed for onametostat in all cell lines ($P < 0.05$), for barasertib in T-98G cells ($P < 0.05$), for CYC116 in U-251 MG cells ($P < 0.05$), and for lomustine in both T-98G and U-87 MG cells ($P < 0.05$ and $P < 0.001$, respectively). In case of MS023 and palbociclib, the trend toward potency increase under hypoxia was evident in all cell lines, yet due to

Compound[a]	Target protein	pIC_{50} in T98-G[b]			pIC_{50} in U-251 MG[b]			pIC_{50} in U-87 MG[b]		
		Normoxia	Hypoxia	P-value[c]	Normoxia	Hypoxia	P-value[c]	Normoxia	Hypoxia	P-value[c]
Azacytidine	DNA methyltransferase 1 and 3 (DNMT1, DNMT3)	5.51 ± 0.09	5.35 ± 0.09	ns	5.61 ± 0.10	5.00 ± 0.14	**	5.88 ± 0.03	5.82 ± 0.04	ns
MS023	Type 1 protein arginine methyltransferases (PRMT)	Below 3.5	Below 3.5	ns	Below 3.5	4.33 ± 0.09	ns	3.92 ± 0.05	4.06 ± 0.06	*
Onametostat	PRMT5	7.16 ± 0.26	8.00 ± 0.25	*	7.12 ± 0.35	7.51 ± 0.50	ns	10.4 ± 0.1	11.4 ± 0.1	***
		4.54 ± 0.10	4.50 ± 0.11	ns	4.48 ± 0.15	5.09 ± 0.11	**	4.75 ± 0.04	4.71 ± 0.05	ns
Tazemetostat	histone-lysine N-methyltransferase enhancer of zeste homolog 2 (EZH2)	Below 3.5	Below 3.5	ns	4.13 ± 0.12	Below 3.5	ns	4.37 ± 0.06	4.20 ± 0.08	*
Vorinostat	Histone deacetylase 1, 2 and 3 (HDAC1, HDAC2, HDAC3)	5.30 ± 0.12	5.22 ± 0.09	ns	5.24 ± 0.10	5.45 ± 0.04	ns	5.87 ± 0.03	5.68 ± 0.04	**
Alisertib	Protein kinase Aurora A (AurA)	8.15 ± 0.24	7.88 ± 0.22	ns	8.34 ± 0.32	8.68 ± 0.56	ns	8.52 ± 0.08	8.42 ± 0.11	ns
		4.76 ± 0.20	4.80 ± 0.27	ns	4.12 ± 0.66	4.61 ± 0.22	ns	5.24 ± 0.11	5.29 ± 0.12	ns
Barasertib[d]	Protein kinase Aurora B (AurB)	5.20 ± 0.05	5.32 ± 0.05	*	7.74 ± 0.20	7.73 ± 0.17	ns	7.85 ± 0.07	7.81 ± 0.18	ns
CYC116	Protein kinases AurA, AurB and vascular endothelial growth factor receptor 2 (VEGFR2)	5.02 ± 0.09	4.84 ± 0.11	ns	4.11 ± 0.14	4.61 ± 0.08	*	5.81 ± 0.04	5.75 ± 0.06	ns
Danusertib	Protein kinases AurA, AurB, AurC	4.81 ± 0.11	4.89 ± 0.16	ns	5.22 ± 0.09	5.02 ± 0.11	ns	6.46 ± 0.03	6.47 ± 0.06	ns
Palbociclib	Protein kinases cyclin-dependent kinases 4 and 6 (CDK4, CDK6)	Below 3.5	4.46 ± 0.14	ns	Below 3.5	3.82 ± 0.19	ns	4.86 ± 0.05	5.03 ± 0.07	**
VX689[d]	Protein kinase AurA	6.23 ± 0.16	6.21 ± 0.14	ns	6.83 ± 0.17	6.49 ± 0.12	ns	6.53 ± 0.03	6.46 ± 0.04	ns
Lomustine	(DNA-alkylating agent)	3.88 ± 0.09	4.07 ± 0.07	*	4.57 ± 0.08	4.57 ± 0.05	ns	4.75 ± 0.03	4.93 ± 0.05	***

Table 1. Viability assay data following incubation of GB cell lines with compounds for 48 h under normoxic or hypoxic conditions. The top part of the table shows data for inhibitors of enzymes carrying out epigenetic modifications and the bottom part of the table for inhibitors of cell cycle-regulating kinases; the control compound lomustine is listed in the last row. pIC_{50} stands for the negative logarithm of the IC_{50} value; the higher is pIC_{50}, the more potent is the compound. [a]For compounds with biphasic dose–response curves, both low-dose and high-dose pIC_{50} values are reported. [b]Standard deviation is shown ($N \geq 3$); pIC_{50} values below 3.5 (corresponding to the IC_{50} values above 316 μM) could not be quantified with sufficient precision due to limitations of the assay. [c]Statistical significance of pairwise comparison for the pIC_{50} obtained under hypoxic *vs* normoxic conditions; *** indicates $P \leq 0.001$, ** indicates $P \leq 0.01$, * indicates $P \leq 0.05$, ns indicates not significant. [d]In case of indicated compounds, biphasic dose–response curves were obtained in at least some of the tested cell lines; however, only the low-dose pIC_{50} value is listed as the high-dose pIC_{50} value possessed large standard deviation.

the generally high IC_{50} values of these compounds, statistical significance could only be confirmed in U-87 MG cells ($P < 0.05$ for MS023 and $P < 0.01$ for palbociclib).

Onametostat affects formation of U-251 MG and U-87 MG spheroids yet does not cause apoptosis

As onametostat showed the most promising trends from the aspect of both low IC_{50} and potency increase in hypoxia, we proceeded with more detailed characterization of this compound. In U-251 MG and U-87 MG cell lines, we explored the effect of onametostat on the formation of tumour spheroids. Increasing concentrations of onametostat (final total concentration of 0.2, 2, or 20 μM) or control compounds (positive control: 50 μM lomustine, negative control: 0.1% DMSO) were added onto the ultra-low attachment microplates together with the cells. The concentrations of onametostat were chosen taking into consideration the trends observed in the viability assay, sufficiently low to avoid the excessive cell death yet sufficiently high to make the effect observable even in 3D culture, which is usually less sensitive to compound treatment than 2D[30–32]. The size of spheroids and the intensity of propidium iodide (PI) staining in necrotic/late apoptotic cells with compromised membrane integrity was assessed after 96 h of incubation. As the inner part of the tumour spheroids permanently resides at the hypoxic conditions due to the limited diffusion of oxygen[33], only normoxic incubation conditions were used.

The results of the assay are summarized in Fig. 3 and Supplementary Fig. S7. In general, the interrupting effect of a compound on the spheroid formation can manifest itself either as decrease of spheroid size (if the compound affects viability and/or proliferation of the cells) or apparent increase of spheroid size (if the compound weakens the cell–cell contacts). Indeed, both trends were evident in our data. In U-251 MG cells, both onametostat and lomustine caused significant increase of the spheroid diameter ($P < 0.05$), with slight dose–response effect observable in case of onametostat (*i.e.*, more concentrated compound resulting in larger apparent diameter). On the other hand, in U-87 MG cells, reduction of spheroid diameter was evident in case of highest onametostat concentration, while lowest concentration of the compound caused apparent increase in spheroid size ($P < 0.001$). Such difference in the cell line behaviour could be explained by the higher proliferation rate but also higher chemosensitivity of the U-87 MG cells, which was also previously observed in the viability assay with the adherent cells (Table 1). Furthermore, increase of the PI staining intensity (normalized by the spheroid area) was observable in U-87 MG spheroids treated with 20 μM onametostat.

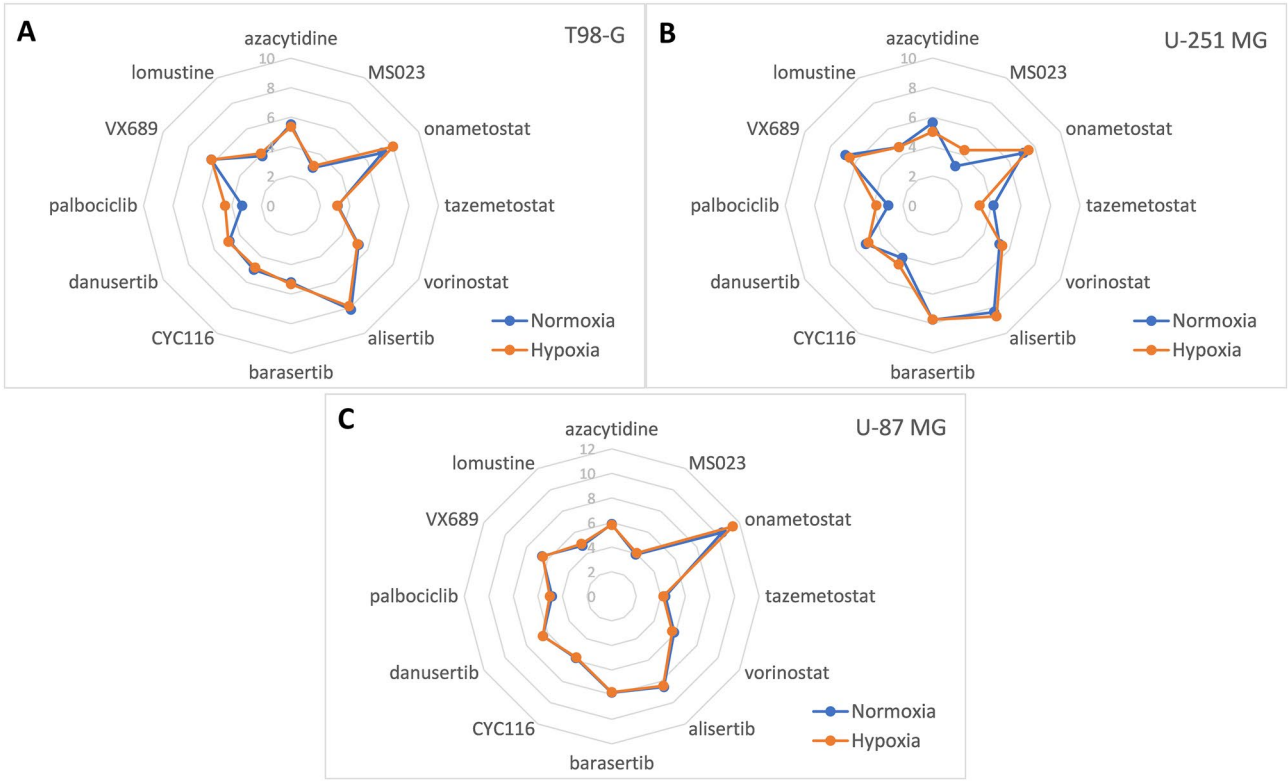

Figure 2. Radar plots enabling comparison of viability pIC_{50} values obtained for different compounds following incubation of cells under normoxic or hypoxic conditions. Cell lines: (**A**) T98-G, (**B**) U-251 MG, (**C**) U-87 MG; the incubation conditions are shown in the right bottom corner. The names of compounds are listed along the radar perimeter. The data was obtained by pooling all independent experiments ($N \geq 3$). For clarity, no error bars are depicted and only one pIC_{50} value is shown per compound (in case of compounds featuring the biphasic dose–response fit, only the largest pIC_{50} value was chosen). The numbering of y-axis is shown in light grey. Please note that the y-scale ranges from 0 to 10 in (**A**,**B**), and from 0 to 12 in (**C**).

Additionally, we explored whether onametostat causes apoptosis in glioblastoma cell lines under normoxic conditions. Increasing concentrations of onametostat (final total concentration of 0.01, 0.1, 1, or 10 μM) or control compound lomustine (50 μM) were added to the U-251 MG, T-98G, or U-87 MG cells transfected with FRET-based biosensor cleavable by caspase-3. The results are summarized in Supplementary Fig. S8. No significant change in FRET was observed in any cell line, indicating that the effect of onametostat is based on other mechanisms than apoptotic cell death. On the other hand, lomustine caused significant change in biosensor FRET, expectedly inducing increase in caspase-3 activity[34] on the scale of some hours after addition of the compound.

Transcriptome studies in T98-G lysates: establishing the characteristic hypoxia and onametostat signatures

As the next part of our experimental effort, we explored the effect of 1 μM onametostat on the transcriptome in T98-G cell line. The adherent cells were incubated with the compound for 48 h under normoxic or hypoxic conditions; as a negative control, 0.1% DMSO was again used. T98-G was chosen as it was overall the least chemosensitive among the cell lines screened in this study (Fig. 2).

For different samples within 3 independent experiments, a read count distribution ranging from 16.8 million to 58.2 million reads was observed. The exhibited read counts were mostly within the interquartile range of 23.3 million to 53.9 million reads, indicating a consistent level of coverage across the majority of the samples (Supplementary Table S2). The t-distributed stochastic neighbor embedding plot (t-SNE; Supplementary Fig. S9) illustrates the clustering based on the similarity of the transcriptome profiles obtained for the different treatments. It was evident that the impact of onametostat treatment is markedly more pronounced than the effect of oxygenation conditions; still, the clustering was distinguishable between the hypoxic vs normoxic conditions, and the independent experiments clustered together.

Figure 4A lists the number of the differentially expressed genes (DEG) in pairwise comparisons of different treatments; FDR rate of 0.05 was used as a cut-off for defining the statistically significant differences. The overall number of both up- and downregulated DEGs was lower in comparisons of cells treated under hypoxic *vs* normoxic conditions than the number of DEGs in comparisons of cells treated with onametostat *vs* DMSO. This was consistent with the more pronounced effect of PRMT5 inhibition as compared to the oxygen deprivation. The number of DEGs common for the various comparisons are shown in the Venn diagram in Fig. 4B. In line with the t-SNE plot, the cells treated with onametostat shared a number of DEGs relative to the DMSO-treated cells

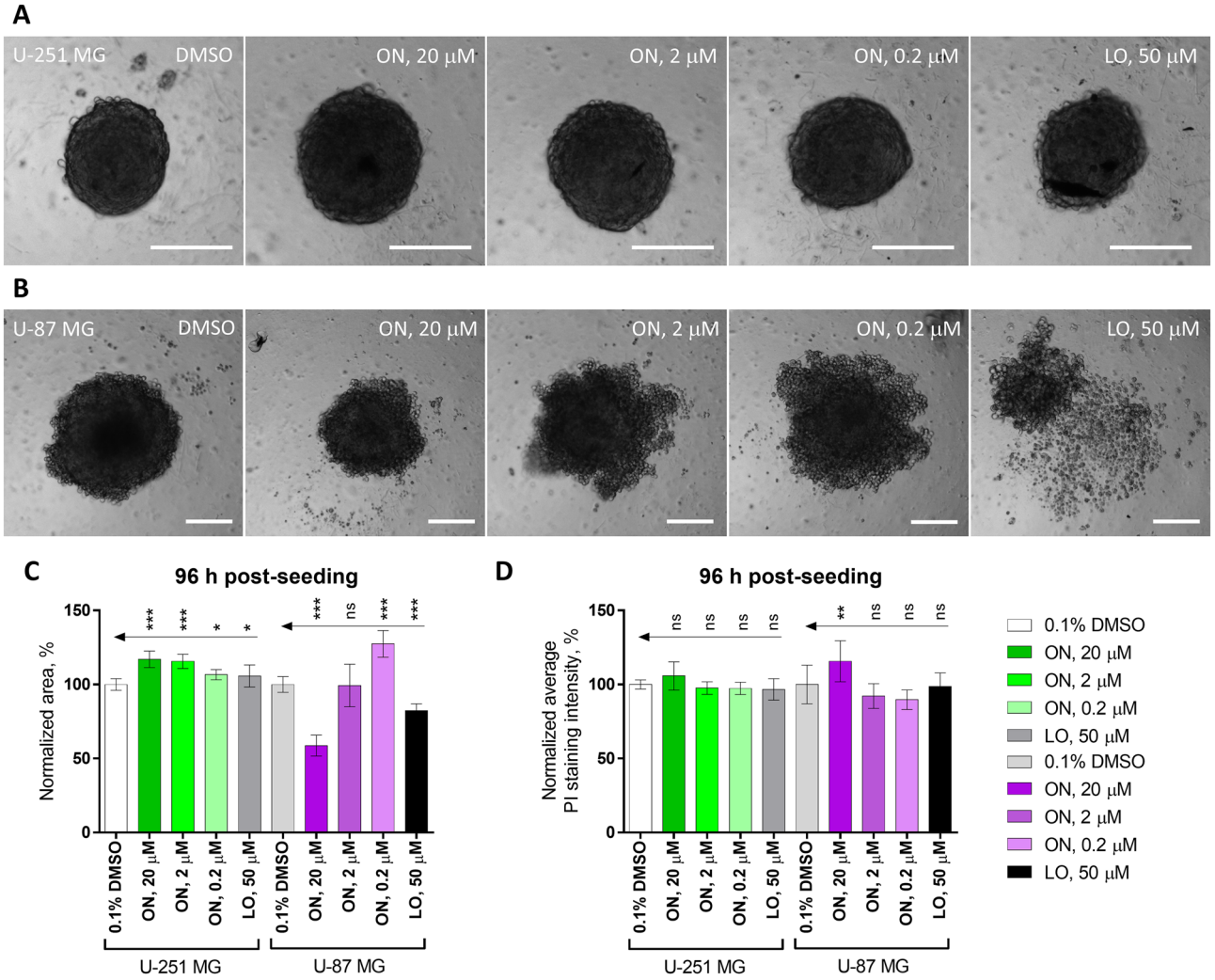

Figure 3. Effect of onametostat (ON) or lomustine (LO) on the spheroid formation in glioblastoma cell lines. (**A**) and (**B**) Show examples of spheroid morphology in U-251 MG cells and U-87 MG cells, respectively, following the 96-h treatment with indicated compounds in a single representative experiment; scale bar: 200 μm. (**C**) Summarizes normalized spheroid area and (**D**) summarizes normalized average intensity of propidium iodide staining per spheroid area using data pooled from 2 independent experiments (a total of 11–12 spheroids per condition); error bars indicate standard deviation. The grouped comparisons show statistical significance of differences for the parameters measured following incubation of cells with onametostat or lomustine *versus* 0.1% DMSO (one-way ANOVA): *** indicates $P \leq 0.001$, ** indicates $P \leq 0.01$, * indicates $P \leq 0.05$, ns indicates not significant.

irrespective of the oxygen content during the treatment. The lists of DEGs termed significant for the different treatment comparisons (FDR < 0.05) are provided in the Supplementary Table S3A–H.

We next focused onto the specific DEGs found for different treatment comparisons. The Volcano plots for comparisons are shown in Fig. 5. The cellular pathways to which the established DEGs belong were analysed using Metascape, an online platform that integrates data from the following ontology sources: KEGG Pathway, GO Biological Processes, Reactome Gene Sets, Canonical Pathways, CORUM, and WikiPathways[28]. The major results are summarized in Supplementary Table S4 and shown in detail in Fig. 6.

Overall, in T98-G cells, 48-h incubation under hypoxic conditions triggered reorganization of the extracellular matrix (e.g., judging by decrease in integrin *ITGA8* in DMSO-treated cells and metalloproteinase *ADAMTS5* in both DMSO- and onametostat-treated cells) and enhanced cell migratory properties (mirrored by increase in atypical chemokine receptor *ACKR3* and neurotrophic receptor *NTRK3* in both treatments). Furthermore, several metabolic processes were altered in hypoxia, as indicated by decrease in expression of cytochrome P450 family members *CYP26B1* and *CYP27C1* in DMSO-treated cells, cytochrome c oxidase *COX8A* in onametostat-treated cells, or retinoic acid responders *RARRES1/2* in both treatments.

Treatment with onametostat also triggered metabolic changes in both normoxic and hypoxic conditions, such as upregulation of expression of glucose-6-phosphate dehydrogenase *H6PD*, mitochondrial dicarboxylate carrier *SLC25A10*, aldo/keto reductase *AKR1A1*, and multiple phosphatidylinositol glycan anchor biosynthesis genes.

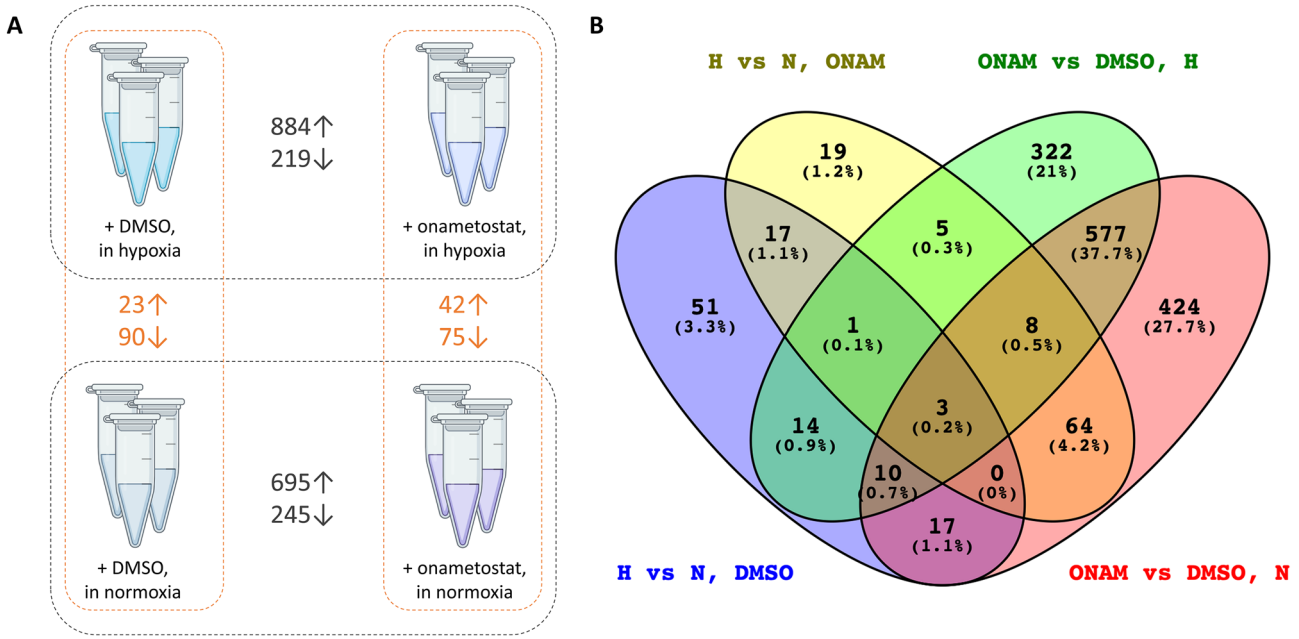

Figure 4. DEG counts in treatment comparisons and number of common DEGs in various treatments. (**A**) Number of DEGs identified as significantly enriched in the pairwise comparisons of differently treated cells (FDR < 0.05); ↑ indicates higher abundance in hypoxia- or onametostat-treated cells and ↓ indicates higher abundance in normoxia- or DMSO-treated cells. (**B**) Venn diagram of the DEGs in various treatment comparisons (FDR < 0.05 in any compared treatments). H, hypoxia; N, normoxia; ONAM, onametostat.

Also, the presence of onametostat reduced expression of various genes regulating activity of transcription factors (e.g., anti-Müllerian hormone *AMH* and interleukin-1 receptor-associated kinase *IRAK2* in both normoxic and hypoxic conditions and homeodomain-interacting kinase *HIPK2* in hypoxic conditions) and suppressed RNA splicing independently of oxygenation status (judging by decrease in expression of small nuclear RNA auxiliary factor *U2AF1*, polypyrimidine tract binding protein *PTBP2*, and several pre-mRNA processing factors). Furthermore, onametostat treatment caused overall downregulation of the signalling pathways sustaining survival of the cancer cells, especially in reduced oxygenation (for instance, decrease in levels of Wnt receptor Frizzled *FZD2* and telomerase *TERT* was significant in hypoxic conditions, while levels of C-X-C motif chemokine *CXCL8* and various mitogen-activated protein kinase cascade members were decreased in both conditions). Finally, several onametostat treatment-related DEGs indicated the cell cycle arrest at G1 phase: e.g., the histone cluster was downregulated in both normoxic and hypoxic conditions[35], the early B-cell transcription factor 4 (*EBF4*) upregulated in both normoxic and hypoxic conditions[36], and the cell cycle inhibitor p21 (*CDKN1A*) upregulated in hypoxic conditions[37].

Onametostat alters levels of cell cycle-related markers and nucleolar proteins in GB cell lines

Based on transcriptomic data in T-98G cell line, we proceeded with validation of the observed trends using immunofluorescent staining in all three GB cell lines following 48-h treatment with onametostat (0.01, 0.1, 1, or 10 μM) or lomustine (50 μM) at normoxic conditions. For validation, we used a set of antibodies recognising several groups of the putatively interesting markers localizing to nuclei of cells. The nuclear localization of all markers was important as we used the previously developed automated detection algorithm that identifies location of cell nuclei from images using the DAPI staining and quantifies the signal of the antibody of interest in the same locations.

The first group of markers included proteins featuring different expression levels dependent on the cell cycle phase: phosho-serine 10 of histone H3 (pS10H3) that is enriched in nuclei at late G2 and on condensed chromosomes in mitosis[38], Aurora A (AurA) that is enriched on condensed chromosomes in mitosis and in nuclei at late G2 and G1[39], cyclin A2 (CCNA2) that locates to nuclei at S[40], and centrosomal protein F (CENPF) that peaks in nuclei from S to early G2 phase[41]. The second group of markers included nucleolar proteins, as some of the RNA splicing-related DEGs downregulated by onametostat (e.g., *U2AF1* and *PRPF3*) are known to be involved in ribosomal biogenesis[42,43], which is carried out in nucleoli. Furthermore, involvement of PRMT5 in small nuclear ribonucleoprotein biogenesis has been reported[44]. For validation, we chose nucleolin (NCL), which is the major nucleolar protein and has been shown to form complex with PRMT5[45], and nuclear mitotic apparatus protein (NuMA), which locates to nucleoli in interphase and mediates the nucleolar stress response[46]. Additionally, in U-251 MG and T-98G cells, we explored the changes in levels of monomethylated Arg3 of human histone H4 (H4R3me1), as the latter is a well-validated substrate of PRMT5[47]. The quantification results are presented in Fig. 7 (data for the cell cycle-related markers) and Supplementary Fig. S10 (data for the nucleolar markers and H4R3me1); the examples of microscopy images showing characteristic immunostaining in non-treated or onametostat-treated cells are shown in Supplementary Figs. S11–17.

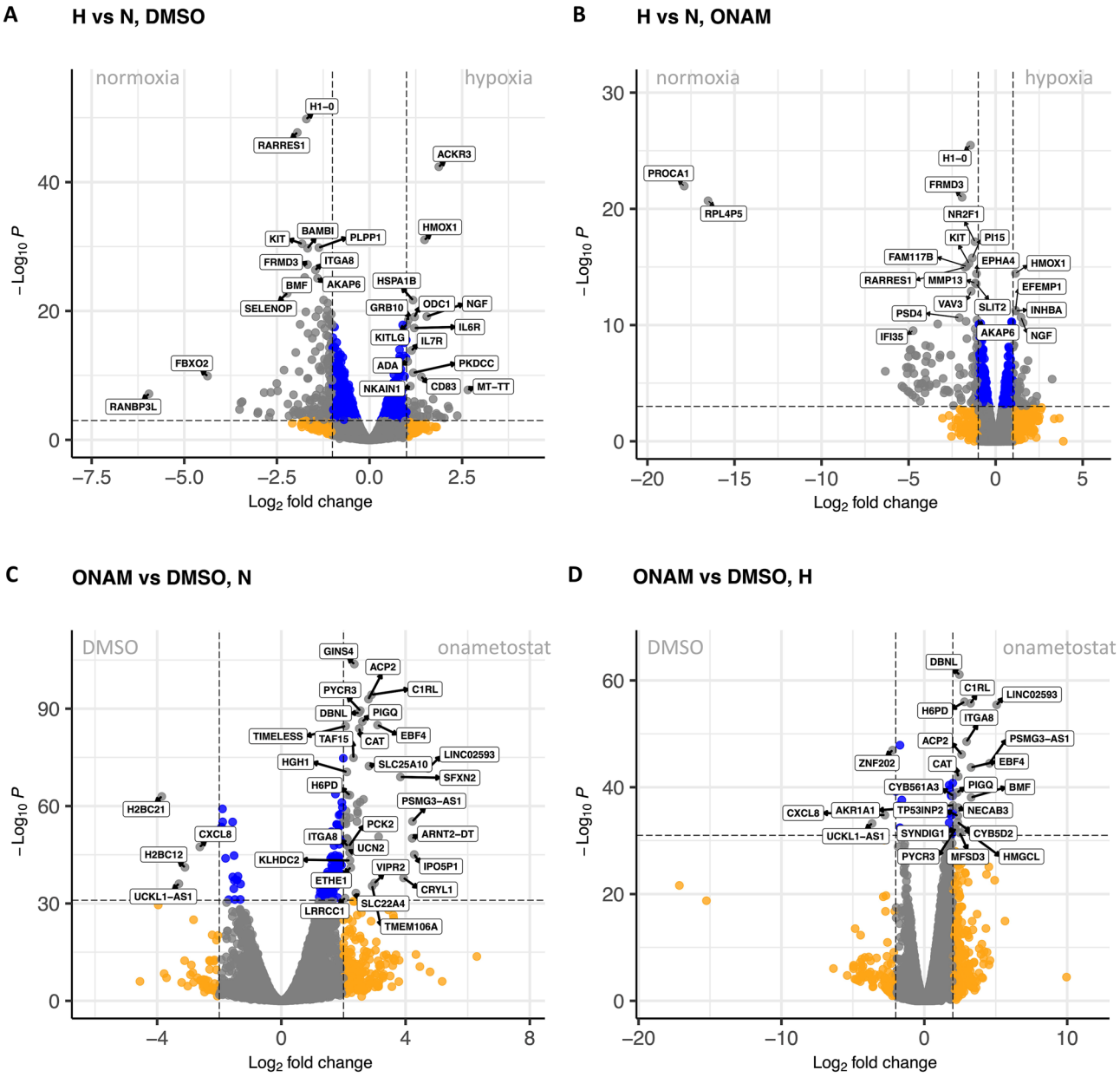

Figure 5. Volcano plots showing DEGs in treatment comparisons. (**A**) Hypoxic *vs* normoxic conditions in the T98-G cells treated with 0.1% DMSO; (**B**) Hypoxic *vs* normoxic conditions in the T98-G cells treated with 1 μM onametostat; (**C**) Onametostat- *vs* DMSO-treated T98-G cells following incubation in normoxia; (**D**) Onametostat- *vs* DMSO-treated T98-G cells following incubation in hypoxia. Top hits are marked with the name labels. In (**A**) and (**B**), DEGs coloured in orange feature binary logarithm of fold change values of below -1 or over 1, and DEGs coloured in blue feature the P-value cut-off of 10^{-3}. In (**C**) and (**D**), DEGs coloured in orange feature binary logarithm of fold change values of below -2 or over 2, and DEGs coloured in blue feature the P-value cut-off of 10^{-32}. H, hypoxia; N, normoxia; ONAM, onametostat.

Interestingly, while treatment with onametostat caused significant alterations of the total intensity of cell cycle marker immunostaining in all tested cell lines ($P < 0.05$), the levels of individual markers fluctuated in a cell line-specific manner. In U-251 MG cells, onametostat did not affect pS10H3 or AurA staining intensity at any concentration yet caused increase in CCNA2 levels at higher concentrations of the compound ($P < 0.01$) and increase in CENPF levels at the highest concentration of compound ($P < 0.001$). In T-98G cells, onametostat caused slight yet statistically significant decrease in pS10H3 and CENPF levels at 1 μM concentration of the compound ($P < 0.001$) and slight yet statistically significant increase in AurA levels at most of the tested concentrations ($P < 0.01$). In U-87 MG cells, all concentrations of onametostat significantly decreased levels of pS10H3 ($P < 0.001$), CCNA2 ($P < 0.001$) and CENPF ($P < 0.05$), while levels of AurA were significantly elevated ($P < 0.001$). The effect of lomustine was more uniform: consistently with the lomustine-induced G2/M arrest reported in literature[48], pS10H3 and AurA levels were significantly elevated in all tested lines ($P < 0.001$). Additionally,

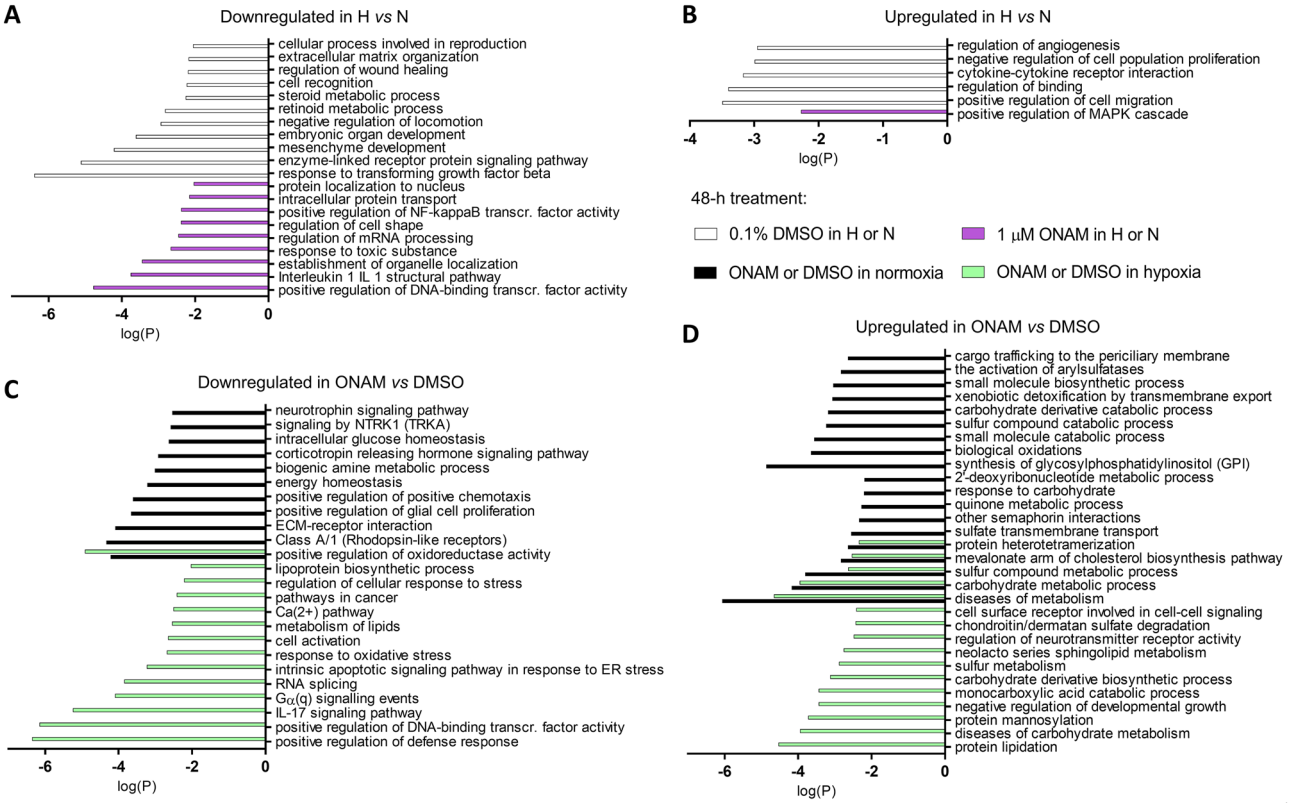

Figure 6. Top cellular pathways identified by the Metascape platform based on the DEGs corresponding to the comparisons of the differently treated samples (FDR < 0.05). The columns indicate decimal logarithms of P-value. (**A**) Pathways downregulated in hypoxic *vs* normoxic conditions; no major overlapping pathways were found between the cells treated with 0.1% DMSO (white columns) or 1 μM onametostat (purple columns). (**B**) Pathways upregulated in hypoxic *vs* normoxic conditions; no major overlapping pathways were found between the cells treated with 0.1% DMSO (white columns) or 1 μM onametostat (purple columns). (**C**) Pathways downregulated in onametostat- *vs* DMSO-treated cells; one major overlapping pathway was found between the cells treated in normoxia (black columns) or hypoxia (light green columns). (**D**) Pathways upregulated in onametostat- *vs* DMSO-treated cells; five major overlapping pathways were found between the cells treated in normoxia (black columns) or hypoxia (light green columns). H, hypoxia; N, normoxia; ONAM, onametostat.

lomustine treatment increased CCNA2 levels in U-87 MG cells ($P < 0.001$) and CENPF levels in U-251 MG as well as T-98G cells ($P < 0.001$).

By contrast, in case of nucleolar markers, a significant decrease of both NCL and NuMA staining was obtained across all tested cell lines upon treatment with all concentrations of onametostat ($P < 0.01$). In line with the DNA-damaging mechanism of lomustine action[49] and the reported involvement of both NCL and NuMA in the DNA damage repair[46,50,51], treatment with lomustine enhanced levels of NCL in all cell lines ($P < 0.001$) and levels of NuMA in T-98G and U-87 MG cells ($P < 0.05$).

Finally, decrease in H4R3me1 levels was confirmed in both tested cell lines. In U-251 MG cells, the reduction of methylation was significant at even 1 nM concentration of onametostat ($P < 0.001$), while in T98-G cells, the inhibitory effect could be quantified at 10 nM concentration of onametostat ($P < 0.01$) yet was pronounced at higher concentrations of compound ($P < 0.001$).

Discussion

The current study served as a follow-up to the previously published effort where the viability profile of GB cell lines U-251 MG (weakly MGMT-positive) and T98-G (strongly MGMT-positive) was established following inhibition of various pathways putatively crucial for the survival of the cancer cells[12]. Here, we expanded the choice of inhibitors targeting the two types of hits identified previously: the cell cycle-regulating kinases and the epigenetic writers or erasers. To provide deeper insight into the variations in compound potency dependent on the tumour- or environment-dictated factors, we additionally included a third cell line and explored the effect of short-term hypoxia treatment (48 h).

The viability assay indicated relatively small effect of hypoxia on the potency of compounds in all tested cell lines, with the largest shift of dose–response curves observed for MS023 in U-251 MG cells, palbociclib in T98-G cells, and onametostat in T98-G cells (all potentiated by hypoxia; see Supplementary Figs. S3–S5). This is in line with the reports on the elevated expression of PRMT5[52,53] and elevated activity of CDK4/6[54,55] under hypoxic conditions.

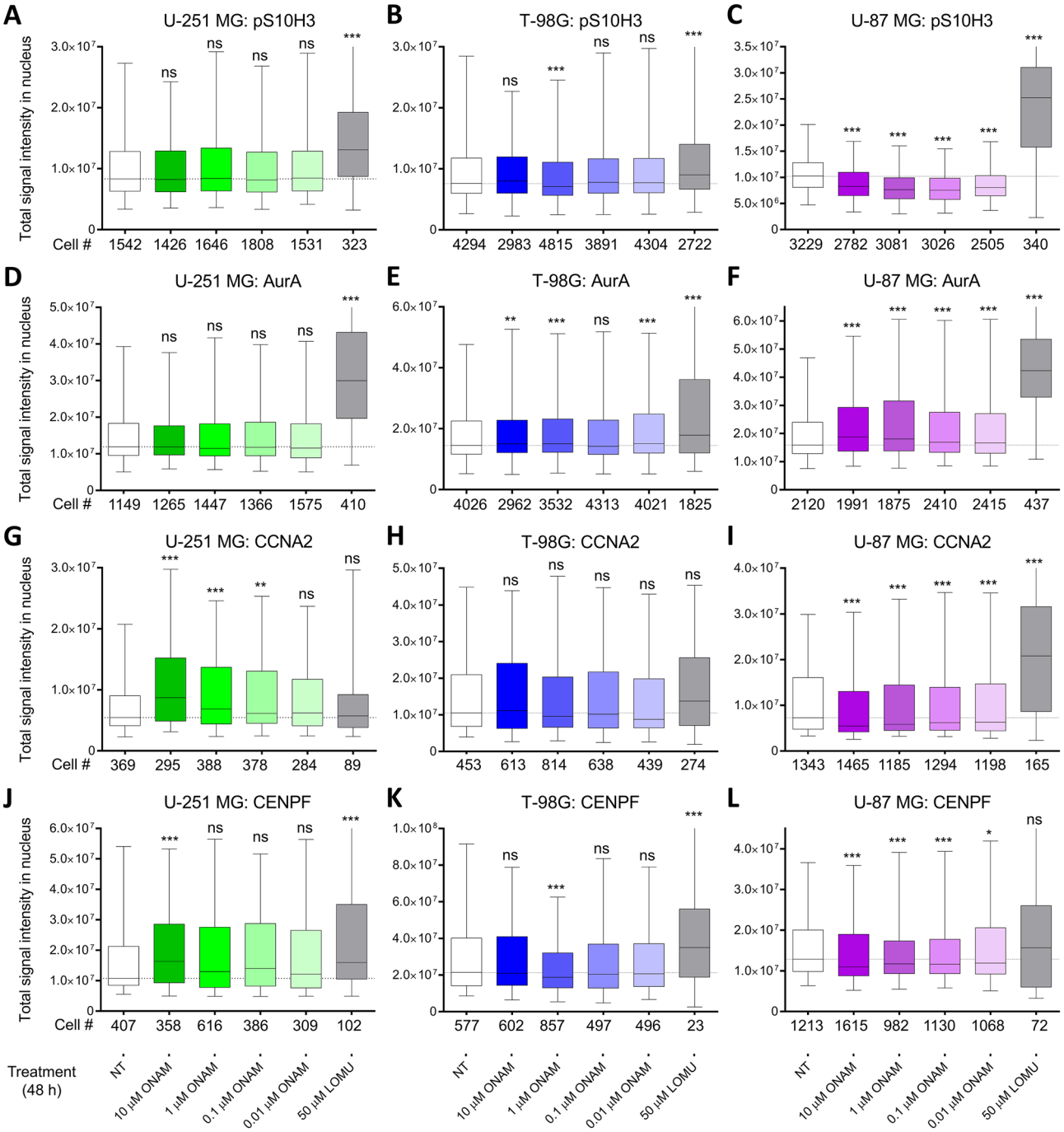

Figure 7. Effect of onametostat (ONAM) or lomustine (LOMU) on the abundance of cell cycle-related markers in nuclei of glioblastoma cell lines. Each box shows the range between the 2nd and 3rd quartile, while the whiskers shown the range between 5 and 95 percentile; thick solid line indicates median of each treatment and thin dotted line in the graph background indicates median of the non-treated cells. Cell lines: data for U-251 MG shown in (**A**,**D**,**G**,**J**); data for T-98G shown in (**B**,**E**,**H**,**K**); data for U-87 MG shown in (**C**,**F**,**I**,**L**). Quantified parameters: total intensity of pS10H3 staining in nucleus shown in (**A**–**C**) (N = 6 for each cell line); total intensity of AurA staining in nucleus shown in (**D**–**F**) (N = 3 for each cell line); total intensity of CCNA2 staining in nucleus shown in (**G**–**I**) (N = 3 for each cell line); total intensity of CENPF staining in nucleus shown in (**J**–**L**) (N = 3 for each cell line). The 48-h treatment conditions are listed at the bottom of the image and the total number of nuclei quantified in case of each condition is shown at the bottom of each panel. The paired comparisons show statistical significance of differences for the parameters measured following incubation of cells with onametostat or lomustine versus non-treated cells (Mann–Whitney U-test): *** indicates $P \le 0.001$, ** indicates $P \le 0.01$, * indicates $P \le 0.05$, ns indicates not significant.

The moderate effect of hypoxic treatment was also observable in case of transcriptome studies in the DMSO-treated T98-G cells (Supplementary Fig. S9). In literature, a recent study in the same cell line reported a substantial number of DEGs following the 72-h hypoxia treatment of passage number 3 cells, with upregulation of the Warburg effect-related genes such as inositol-requiring enzyme 1 (*IRE1*) or lactate dehydrogenase A (*LDHA*)[56]. Neither *IRE1* nor *LDHA* were identified as DEGs in our study, which may be explained by the shorter treatment times and higher cell passage number in our experiments. The longer culturing of cells was chosen due to our previous observation that in case of lower passages (below number 4), the proliferation rate of the cells changes remarkably (mirrored by the apparent drop in efficacy of the Aurora A inhibitors)[16], and we thus chose later passages (number 8–9) for the transcriptomic study to minimize the putative effect of the proliferation rate change.

Still, several DEGs short-listed in our study (Supplementary Tables S3, S4) have been previously linked to hypoxia. Among the genes upregulated in hypoxia in both DMSO- and onametostat-treated cells, the atypical chemokine receptor 3 (*ACKR3*) has been explored in the context of cardiovascular diseases and inflammation[57], the nerve growth factor (*NGF*) in the context of angiogenesis in non-small cell lung cancer[58], and the 4-hydroxyphenylpyruvate dioxygenase (*HPD*) in the context of metabolic reprogramming in lung cancer[59]. In case of the hypoxia-upregulated DEGs found only in the DMSO-treated cells, the heme oxygenase-1 (*HMOX1*) and isthmin1 (*ISM1*) have been reported as the direct downstream targets of the hypoxia-inducible transcription factor (HIF)[60,61], whereas indirect regulation mechanism by HIF has been proposed for the C-X-C motif chemokine ligand 3 (*CXCL3*)[62]. From the hypoxia-induced pathways identified by the Metascape algorithm (Fig. 6 and Supplementary Table S4), upregulation of the cytokine stimulation and increase of cell migratory properties as well as remodelling of the extracellular matrix can be directly linked to inflammation and metastasis formation in cancer[63,64]. Somewhat surprisingly, Metascape also identified the cluster corresponding to the response to transforming growth factor β (TGF-β) among the pathways downregulated under hypoxic conditions in our study. In general, HIF is known to activate the TGF-β signalling[65]—thus, our current finding might point to reorganization rather than suppression of the pathway under hypoxic conditions.

Among the tested compounds that affected the cell viability at two-digit nanomolar or lower concentration in both normoxia and hypoxia across the cell lines (Table 1), we chose PRMT5 inhibitor onametostat as the compound of interest for the further studies. According to literature, inhibition of PRMT5 has been termed an efficient strategy in cancers featuring deletion of the methylthioadenosine phosphorylase gene (*MTAP*), as such cancers rely on PRMT5 for survival[66]. Importantly, in GB, *MTAP* is one of the most frequently deleted genes[67]—although it has been shown that the success of PRMT5 inhibition in the context of GB is also dependent on other factors[68]. Still, PRMT5 inhibitors are increasingly studied in the context of both GB cell lines and primary cells[68,69], and some reports also indicate inverse correlation between the PRMT5 expression levels and survival of patients with glioma or GB diagnosis[70,71].

While we are not aware of previous reports on the effect of onametostat on the GB cell line transcriptome, the list of DEGs in onametostat- *vs* DMSO-treated cells revealed several players previously reported as characteristic of PRMT5 inhibition (Supplementary Tables S3, S4). For instance, PRMT5 is known to regulate DNA repair and mRNA splicing[72], both of which were short-listed as downregulated pathways in our data by the Metascape algorithm. Among the DEGs belonging to the mRNA splicing pathway, polypyrimidine tract-binding protein 2 (*PTBP2*) and U2 small nuclear RNA auxiliary factor 1 (*U2AF1*) have been previously shown to promote proliferation in glioma[73,74]. The altered expression of several other genes following the treatment of T98-G cells with onametostat in both normoxic and hypoxic conditions also indicated interference of the compound with the cancer survival strategies. Among the downregulated DEGs, the pleckstrin homology domain containing S1 (*PLEKHS1*) and the cluster representing the IL-17-regulated genes are of interest as these can be linked to the PI3K/Akt pathway[75,76], which is frequently mutated in various solid cancers, including GB[77]. Additionally, the semaphorins 5A and 6A (*SEMA5A*, *SEMA6A*) which we identified among the upregulated DEGs have been shown to act as the potential suppressors of cancer migration[78,79].

The elevation of the cell cycle arrest markers observed in transcriptomic study with T-98G cells was in line with the biphasic dose–response curves of onametostat observed in viability assay for all cell lines (Supplementary Figs. S3C, S4C, S5C), as the low-dose effect is frequently indicative of cytostatic rather than cytotoxic effects[16]. Based on the IF data regarding changes in nuclear levels of cell cycle-related markers (Fig. 7), it is likely that onametostat synchronized T-98 G and U-87 MG cells in the G1 phase and U-251 MG in the S phase of cell cycle, although further validation of these trends by flow cytometry or other relevant methodologies is required. The absence of apoptotic effect of onametostat in all cell lines under normoxic conditions (Supplementary Fig. S8) also indirectly confirmed the cytostatic properties of the compound—although further studies should explore whether onametostat induces autophagy in GB, as autophagy has been shown to dictate sensitivity towards PRMT5 inhibition in other cancer types[53,80].

Finally, several of the onametostat-upregulated DEGs highlighted the survival strategies of GB and cancer in general, as the post-treatment transcriptome inevitably included the gene pool from the surviving population of the T98-G cells. Such DEGs, found upregulated in both normoxic and hypoxic conditions, include hexose-6-phosphate dehydrogenase (*H6PD*) that contributes to metabolic reprogramming in glioma stem cells[81], protein tyrosine kinase 2β (*PTK2B*) that enhances glioma cell migration[82], and catalase (*CAT*) that regulates chemo- and radioresistance in glioblastoma[83]. Our short-list of DEGs did not contain the microtubule regulator stathmin 2 that was reported as the PRMT5 inhibitor resistance-promoting player in a different cancer context (lung adenocarcinoma)[84]. However, we found that another microtubule-related molecular target was upregulated by onametostat under hypoxic conditions (microtubule-associated serine/threonine kinase 1, *MAST1*), which has also previously been linked to the putative resistance mechanisms in cancer[85].

The given study was limited to the in vitro settings, and our major findings—whether related to sensitivity or resistance mechanisms—should thus be confirmed in clinically more relevant models. Other limitations include absence of mRNA sequencing data for all cell lines used in the study and lack of validation of the observed

trends by RT-qPCR or Western blot. We have also not addressed the blood–brain barrier (BBB)-penetrative properties of the tested compounds. However, it has been shown that the integrity of BBB is disrupted following radiotherapy[86,87], which can be utilized for development of combined treatment schemes. As onametostat induces cell cycle arrest at the G1 phase, which represents the less sensitive cell cycle phase to radiotherapy[88,89], it is not advisable to apply it prior to radiation, but rather following the latter. Furthermore, despite the emergence of DEGs indicating resistance to onametostat in our transcriptome study, it is worth to investigate effect of mixtures of onametostat with lomustine for achieving improved effect on proliferation of GB cells at low doses of the PRMT5 inhibitor. Overall, we confirmed that inhibition of PRMT5 is a promising strategy that should be explored more intensely in the context of treatment of recurrent glioblastoma.

Data availability

The mRNA sequencing raw data are available in Gene Expression Omnibus (GEO) at https://www.ncbi.nlm.nih.gov/geo/ and can be accessed with GEO accession number: GSE235648. The Aparecium software and Ilastik model are available at https://gpcr.ut.ee/aparecium.html. Other datasets generated and analysed during the current study are available from the corresponding author on reasonable request.

Received: 25 July 2023; Accepted: 15 February 2024
Published online: 21 February 2024

References

1. Stupp, R. *et al.* Radiotherapy plus concomitant and adjuvant temozolomide for glioblastoma. *N. Engl. J. Med.* **352**, 987–996 (2005).
2. Wick, W. *et al.* Phase III study of enzastaurin compared with lomustine in the treatment of recurrent intracranial glioblastoma. *J. Clin. Oncol.* **28**, 1168–1174 (2010).
3. Batchelor, T. T. *et al.* Phase III randomized trial comparing the efficacy of cediranib as monotherapy, and in combination with lomustine, versus lomustine alone in patients with recurrent glioblastoma. *J. Clin. Oncol.* **31**, 3212–3218 (2013).
4. Taal, W. *et al.* Single-agent bevacizumab or lomustine versus a combination of bevacizumab plus lomustine in patients with recurrent glioblastoma (BELOB trial): A randomised controlled phase 2 trial. *Lancet Oncol.* **15**, 943–953 (2014).
5. Kazmi, F., Soon, Y. Y., Leong, Y. H., Koh, W. Y. & Vellayappan, B. Re-irradiation for recurrent glioblastoma (GBM): A systematic review and meta-analysis. *J. Neurooncol.* **142**, 79–90 (2019).
6. Friedman, H. S. *et al.* Bevacizumab alone and in combination with irinotecan in recurrent glioblastoma. *JCO* **27**, 4733–4740 (2009).
7. Lombardi, G. *et al.* Regorafenib compared with lomustine in patients with relapsed glioblastoma (REGOMA): A multicentre, open-label, randomised, controlled, phase 2 trial. *Lancet Oncol.* **20**, 110–119 (2019).
8. Louis, D. N. *et al.* The 2021 WHO Classification of Tumors of the Central Nervous System: A summary. *Neuro Oncol.* **23**, 1231–1251 (2021).
9. Colwell, N. *et al.* Hypoxia in the glioblastoma microenvironment: Shaping the phenotype of cancer stem-like cells. *Neuro-Oncol.* **19**, 887–896 (2017).
10. Monteiro, A. R., Hill, R., Pilkington, G. J. & Madureira, P. A. The role of hypoxia in glioblastoma invasion. *Cells* **6**, 45 (2017).
11. Macharia, L. W. *et al.* The genotypic and phenotypic impact of hypoxia microenvironment on glioblastoma cell lines. *BMC Cancer* **21**, 1248 (2021).
12. Lavogina, D., Laasfeld, T., Vardja, M., Lust, H. & Jaal, J. Viability fingerprint of glioblastoma cell lines: Roles of mitotic, proliferative, and epigenetic targets. *Sci. Rep.* **11**, 20338 (2021).
13. Xu, H. *et al.* The nanoprodrug of polytemozolomide combines with MGMT siRNA to enhance the effect of temozolomide in glioma. *Drug Deliv.* **30**, 1–13 (2023).
14. Naidu, M. D., Mason, J. M., Pica, R. V., Fung, H. & Peña, L. A. Radiation resistance in glioma cells determined by DNA damage repair activity of Ape1/Ref-1. *J. Radiat. Res.* **51**, 393–404 (2010).
15. Rahnel, H. *et al.* A selective biligand inhibitor of CK2 increases caspase-3 activity in cancer cells and inhibits platelet aggregation. *ChemMedChem* **12**, 1723–1736 (2017).
16. Lavogina, D. *et al.* Revisiting the resazurin-based sensing of cellular viability: Widening the application horizon. *Biosensors* **12**, 196 (2022).
17. Saar, M. *et al.* Exploring the molecular players behind the potentiation of chemotherapy effects by durvalumab in lung adenocarcinoma cell lines. *Pharmaceutics* **15**, 1485 (2023).
18. Schindelin, J. *et al.* Fiji: An open-source platform for biological-image analysis. *Nat. Methods* **9**, 676–682 (2012).
19. Brown, J., Pirrung, M. & McCue, L. A. FQC Dashboard: Integrates FastQC results into a web-based, interactive, and extensible FASTQ quality control tool. *Bioinformatics* **33**, 3137–3139 (2017).
20. Ewels, P., Magnusson, M., Lundin, S. & Käller, M. MultiQC: Summarize analysis results for multiple tools and samples in a single report. *Bioinformatics* **32**, 3047–3048 (2016).
21. Chen, S., Zhou, Y., Chen, Y. & Gu, J. fastp: An ultra-fast all-in-one FASTQ preprocessor. *Bioinformatics* **34**, i884–i890 (2018).
22. Dobin, A. *et al.* STAR: Ultrafast universal RNA-seq aligner. *Bioinformatics* **29**, 15–21 (2013).
23. Liao, Y., Smyth, G. K. & Shi, W. featureCounts: An efficient general purpose program for assigning sequence reads to genomic features. *Bioinformatics* **30**, 923–930 (2014).
24. R Core Team. R: The R Project for Statistical Computing. https://www.r-project.org/ (2018).
25. Love, M. I., Huber, W. & Anders, S. Moderated estimation of fold change and dispersion for RNA-seq data with DESeq2. *Genome Biol.* **15**, 550 (2014).
26. Robinson, M. D., McCarthy, D. J. & Smyth, G. K. edgeR: A bioconductor package for differential expression analysis of digital gene expression data. *Bioinformatics* **26**, 139–140 (2010).
27. Oliveiros, J. C. Venny 2.1.0. *Venny. An interactive tool for comparing lists with Venn's diagrams* https://bioinfogp.cnb.csic.es/tools/venny/index.html (2007).
28. Zhou, Y. *et al.* Metascape provides a biologist-oriented resource for the analysis of systems-level datasets. *Nat. Commun.* **10**, 1523 (2019).
29. Veiksina, S. *et al.* Fluorescence anisotropy-based assay for characterization of ligand binding dynamics to GPCRs: The case of Cy3B-labeled ligands binding to MC4 receptors in budded baculoviruses. In *G Protein-Coupled Receptor Screening Assays: Methods and Protocols* (eds Martins, S. A. M. & Prazeres, D. M. F.) 119–136 (Springer US, 2021). https://doi.org/10.1007/978-1-0716-1221-7_8.
30. Breslin, S. & O'Driscoll, L. The relevance of using 3D cell cultures, in addition to 2D monolayer cultures, when evaluating breast cancer drug sensitivity and resistance. *Oncotarget* **7**, 45745–45756 (2016).
31. Melissaridou, S. *et al.* The effect of 2D and 3D cell cultures on treatment response, EMT profile and stem cell features in head and neck cancer. *Cancer Cell Int.* **19**, 16 (2019).

32. Muguruma, M. *et al.* Differences in drug sensitivity between two-dimensional and three-dimensional culture systems in triple-negative breast cancer cell lines. *Biochem. Biophys. Res. Commun.* **533**, 268–274 (2020).
33. Grimes, D. R., Kelly, C., Bloch, K. & Partridge, M. A method for estimating the oxygen consumption rate in multicellular tumour spheroids. *J. R. Soc. Interface* **11**, 20131124 (2014).
34. Yamamuro, S. *et al.* Lomustine and nimustine exert efficient antitumor effects against glioblastoma models with acquired temozolomide resistance. *Cancer Sci.* **112**, 4736–4747 (2021).
35. Su, C. *et al.* DNA damage induces downregulation of histone gene expression through the G1 checkpoint pathway. *EMBO J.* **23**, 1133–1143 (2004).
36. Liao, D. Emerging roles of the EBF family of transcription factors in tumor suppression. *Mol. Cancer Res.* **7**, 1893–1901 (2009).
37. Dutto, I., Tillhon, M., Cazzalini, O., Stivala, L. A. & Prosperi, E. Biology of the cell cycle inhibitor p21(CDKN1A): Molecular mechanisms and relevance in chemical toxicology. *Arch. Toxicol.* **89**, 155–178 (2015).
38. Crosio, C. *et al.* Mitotic phosphorylation of histone H3: Spatio-temporal regulation by mammalian aurora kinases. *Mol. Cell Biol.* **22**, 874–885 (2002).
39. Naso, F. D. *et al.* Nuclear localisation of Aurora-A: Its regulation and significance for Aurora-A functions in cancer. *Oncogene* **40**, 3917–3928 (2021).
40. Silva Cascales, H. *et al.* Cyclin A2 localises in the cytoplasm at the S/G2 transition to activate PLK1. *Life Sci. Alliance* **4**, e202000980 (2021).
41. Loftus, K. M. *et al.* Mechanism for G2 phase-specific nuclear export of the kinetochore protein CENP-F. *Cell Cycle* **16**, 1414–1429 (2017).
42. Akef, A., McGraw, K., Cappell, S. D. & Larson, D. R. Ribosome biogenesis is a downstream effector of the oncogenic U2AF1-S34F mutation. *PLoS Biol.* **18**, e3000920 (2020).
43. Comitato, A. *et al.* Mutations in splicing factor PRPF3, causing retinal degeneration, form detrimental aggregates in photoreceptor cells. *Hum. Mol. Genet.* **16**, 1699–1707 (2007).
44. Guderian, G. *et al.* RioK1, a new interactor of protein arginine methyltransferase 5 (PRMT5), competes with pICln for binding and modulates PRMT5 complex composition and substrate specificity. *J. Biol. Chem.* **286**, 1976–1986 (2011).
45. Teng, Y. *et al.* AS1411 alters the localization of a complex containing protein arginine methyltransferase 5 and nucleolin. *Cancer Res.* **67**, 10491–10500 (2007).
46. Jayaraman, S. *et al.* The nuclear mitotic apparatus protein NuMA controls rDNA transcription and mediates the nucleolar stress response in a p53-independent manner. *Nucleic Acids Res.* **45**, 11725–11742 (2017).
47. Zhao, Q. *et al.* PRMT5-mediated methylation of histone H4R3 recruits DNMT3A, coupling histone and DNA methylation in gene silencing. *Nat. Struct. Mol. Biol.* **16**, 304–311 (2009).
48. Harvey, K. A. *et al.* Enhanced anticancer properties of lomustine in conjunction with docosahexaenoic acid in glioblastoma cell lines. *J. Neurosurg.* **122**, 547–556 (2015).
49. Chakkath, T., Lavergne, S., Fan, T. M., Bunick, D. & Dirikolu, L. Alkylation and carbamylation effects of lomustine and its major metabolites and MGMT expression in canine cells. *Vet. Sci.* **2**, 52–68 (2015).
50. Scott, D. D. & Oeffinger, M. Nucleolin and nucleophosmin: Nucleolar proteins with multiple functions in DNA repair. *Biochem. Cell Biol.* **94**, 419–432 (2016).
51. El-Khamisy, S. F. Oxidative DNA damage and repair at non-coding regulatory regions. *Trends Cell Biol.* **33**, 939–949 (2023).
52. Zheng, Y. *et al.* PRMT5 facilitates angiogenesis and EMT via HIF-1α/VEGFR/Akt signaling axis in lung cancer. *Aging* **15**, 6163–6178 (2023).
53. Fan, J. *et al.* The PRMT5 inhibitor C9 mitigates hypoxia-induced carboplatin resistance in lung cancer by inducing autophagy. *Cell Biol. Int.* **47**, 1702–1715 (2023).
54. Warfel, N. A. Targeting CDK4/6 to oppose hypoxia-mediated therapeutic resistance. *Cell Cycle* **16**, 1241–1242 (2017).
55. Zhang, J., Zhou, L., Zhao, S., Dicker, D. T. & El-Deiry, W. S. The CDK4/6 inhibitor palbociclib synergizes with irinotecan to promote colorectal cancer cell death under hypoxia. *Cell Cycle* **16**, 1193–1200 (2017).
56. White, B. E., Liu, Y., Hakonarson, H. & Buono, R. J. RNA sequencing in hypoxia-adapted T98G glioblastoma cells provides supportive evidence for IRE1 as a potential therapeutic target. *Genes* **14**, 841 (2023).
57. Duval, V., Alayrac, P., Silvestre, J.-S. & Levoye, A. Emerging roles of the atypical chemokine receptor 3 (ACKR3) in cardiovascular diseases. *Front. Endocrinol.* **13**, 906586 (2022).
58. Lu, Q.-L., Liu, J., Zhu, X.-L. & Xu, W.-J. Expression of nerve growth factor and hypoxia inducible factor-1α and its correlation with angiogenesis in non-small cell lung cancer. *J. Huazhong Univ. Sci. Technol. Med. Sci.* **34**, 359–362 (2014).
59. Shan, C. *et al.* 4-hydroxyphenylpyruvate dioxygenase promotes lung cancer growth via pentose phosphate pathway (PPP) flux mediated by LKB1-AMPK/HDAC10/G6PD axis. *Cell Death Dis.* **10**, 1–13 (2019).
60. Dunn, L. L. *et al.* Hmox1 (Heme Oxygenase-1) Protects Against Ischemia-Mediated Injury via Stabilization of HIF-1α (Hypoxia-Inducible Factor-1α). *Arterioscler Thromb Vasc Biol* **41**, 317–330 (2021).
61. Li, J. *et al.* Novel HIF-1-target gene isthmin1 contributes to hypoxia-induced hyperpermeability of pulmonary microvascular endothelial cells monolayers. *Am. J. Physiol. Cell Physiol.* **321**, C671–C680 (2021).
62. Korbecki, J. *et al.* The effect of hypoxia on the expression of CXC chemokines and CXC chemokine receptors—A review of literature. *Int. J. Mol. Sci.* **22**, 843 (2021).
63. Castillo-Rodríguez, R. A., Trejo-Solís, C., Cabrera-Cano, A., Gómez-Manzo, S. & Dávila-Borja, V. M. Hypoxia as a modulator of inflammation and immune response in cancer. *Cancers* **14**, 2291 (2022).
64. Saxena, K., Jolly, M. K. & Balamurugan, K. Hypoxia, partial EMT and collective migration: Emerging culprits in metastasis. *Transl. Oncol.* **13**, 100845 (2020).
65. Mingyuan, X. *et al.* Hypoxia-inducible factor-1α activates transforming growth factor-β1/Smad signaling and increases collagen deposition in dermal fibroblasts. *Oncotarget* **9**, 3188–3197 (2017).
66. Smith, C. R. *et al.* Fragment-based discovery of MRTX1719, a synthetic lethal inhibitor of the PRMT5·MTA complex for the treatment of MTAP-deleted cancers. *J. Med. Chem.* **65**, 1749–1766 (2022).
67. Suzuki, T. *et al.* Genetic analysis of human glioblastomas using a genomic microarray system. *Brain Tumor Pathol.* **21**, 27–34 (2004).
68. Sachamitr, P. *et al.* PRMT5 inhibition disrupts splicing and stemness in glioblastoma. *Nat. Commun.* **12**, 979 (2021).
69. Banasavadi-Siddegowda, Y. K. *et al.* Targeting protein arginine methyltransferase 5 sensitizes glioblastoma to trametinib. *Neurooncol. Adv.* **4**, vdac095 (2022).
70. Han, X. *et al.* Expression of PRMT5 correlates with malignant grade in gliomas and plays a pivotal role in tumor growth in vitro. *J. Neurooncol.* **118**, 61–72 (2014).
71. Yan, F. *et al.* Genetic validation of the protein arginine methyltransferase PRMT5 as a candidate therapeutic target in glioblastoma. *Cancer Res.* **74**, 1752–1765 (2014).
72. Liang, Z., Wen, C., Jiang, H., Ma, S. & Liu, X. Protein arginine methyltransferase 5 functions via interacting proteins. *Front. Cell Dev. Biol.* **9**, 725301 (2021).
73. Cheung, H. C. *et al.* Splicing factors PTBP1 and PTBP2 promote proliferation and migration of glioma cell lines. *Brain* **132**, 2277–2288 (2009).

74. Li, G. *et al.* Circ-U2AF1 promotes human glioma via derepressing neuro-oncological ventral antigen 2 by sponging hsa-miR-7-5p. *J. Cell Physiol.* **234**, 9144–9155 (2019).
75. Xing, X. *et al.* PLEKHS1 over-expression is associated with metastases and poor outcomes in papillary thyroid carcinoma. *Cancers* **12**, 2133 (2020).
76. Zheng, Q. *et al.* IL-17A promotes cell migration and invasion of glioblastoma cells via activation of PI3K/AKT signalling pathway. *J. Cell Mol. Med.* **23**, 357–369 (2019).
77. Kandoth, C. *et al.* Mutational landscape and significance across 12 major cancer types. *Nature* **502**, 333–339 (2013).
78. Saxena, S., Purohit, A., Varney, M. L., Hayashi, Y. & Singh, R. K. Semaphorin-5A maintains epithelial phenotype of malignant pancreatic cancer cells. *BMC Cancer* **18**, 1283 (2018).
79. Chen, L.-H., Liao, C.-Y., Lai, L.-C., Tsai, M.-H. & Chuang, E. Y. Semaphorin 6A attenuates the migration capability of lung cancer cells via the NRF2/HMOX1 axis. *Sci. Rep.* **9**, 13302 (2019).
80. Brobbey, C. *et al.* Autophagy dictates sensitivity to PRMT5 inhibitor in breast cancer. *Sci. Rep.* **13**, 10752 (2023).
81. Xu, X. *et al.* Rewiring of purine metabolism in response to acidosis stress in glioma stem cells. *Cell Death Dis.* **12**, 277 (2021).
82. Lipinski, C. A. *et al.* The tyrosine kinase pyk2 promotes migration and invasion of glioma cells. *Neoplasia* **7**, 435–445 (2005).
83. Flor, S. *et al.* Catalase overexpression drives an aggressive phenotype in glioblastoma. *Antioxidants* **10**, 1988 (2021).
84. Mueller, H. S. *et al.* Acquired resistance to PRMT5 inhibition induces concomitant collateral sensitivity to paclitaxel. *Proc. Natl. Acad. Sci. USA* **118**, e2024055118 (2021).
85. Jin, L. *et al.* MAST1 drives cisplatin resistance in human cancers by rewiring cRaf independent MEK activation. *Cancer Cell* **34**, 315-330.e7 (2018).
86. Hart, E. *et al.* Blood-brain barrier permeability following conventional photon radiotherapy—A systematic review and meta-analysis of clinical and preclinical studies. *Clin. Transl. Radiat. Oncol.* **35**, 44–55 (2022).
87. Chacko, A.-M. *et al.* Targeted delivery of antibody-based therapeutic and imaging agents to CNS tumors: Crossing the blood-brain-barrier divide. *Expert Opin. Drug Deliv.* **10**, 907–926 (2013).
88. Biade, S., Stobbe, C. C. & Chapman, J. D. The intrinsic radiosensitivity of some human tumor cells throughout their cell cycles. *Radiat. Res.* **147**, 416–421 (1997).
89. Pawlik, T. M. & Keyomarsi, K. Role of cell cycle in mediating sensitivity to radiotherapy. *Int. J. Radiat. Oncol. Biol. Phys.* **59**, 928–942 (2004).

Acknowledgements

We thank Ago Rinken group members for the maintenance of the microplate reader and microscopy platform. We are also grateful to BEA, the Bioinformatics and Expression Analysis core facility that is supported by the board of research at the Karolinska Institute.

Author contributions

Conceptualization, D.L. and J.J.; Methodology, D.L., M.K.K., K.-L.E. and V.M.; Validation, D.L., M.K.K., H.V., V.D.N. and H.L.; Formal analysis, D.L. and M.K.K.; Resources, D.L., V.D.N., A.S. and J.J.; Writing—original draft preparation, D.L., V.M. and V.D.N.; Writing—review and editing, D.L., M.K.K., H.V., V.M., V.D.N., H.L., K.-L.E., A.S. and J.J.; Visualization, D.L. and V.M.; Supervision, D.L., K.-L.E., A.S. and J.J.; Project administration, A.S. and J.J.; Funding acquisition, A.S. and J.J.

Funding

The study was supported by the internal financing from the Institute of Clinical Medicine, University of Tartu, Estonia (PMVCMHO), by the Estonian Ministry of Education and Research and the Estonian Research Council (PRG454, PRG1076, PUT1077), by the European Regional Development Fund (2014–2020.4.01.15-0012), and by Horizon 2020 innovation grant (ERIN, grant no. EU952516).

Competing interests

The authors declare no competing interests.

Additional information

Supplementary Information The online version contains supplementary material available at https://doi.org/10.1038/s41598-024-54707-4.

Correspondence and requests for materials should be addressed to D.L. or J.J.